International Journal of Solids and Structures 343 (2027) 114424

Contents lists available at ScienceDirect

International Journal of Solids and Structures

journal homepage: www.elsevier.com/locate/ijsolstr

Pressure-induced buckling and inversion of oval shells

Haesoo Park [a,1], Yuseong Song [b,1], Kanghyun Ki [c], Anna Lee [b,*], Jonghyun Ha [a,*]

[a] Department of Mechanical Engineering, Ajou University, Suwon, Gyeonggi-Do 16499, South Korea
[b] Department of Mechanical Engineering, Pohang University of Science and Technology (POSTECH), 77 Cheongam-ro, Nam-gu, Pohang, Gyeongsangbuk-Do 37673, South Korea
[c] Advanced Aeroengine Research Team, Korea Aerospace Research Institute, Gwahak-Ro 169-84, Yuseong-Gu, Daejeon 34133, South Korea

ARTICLE INFO

Keywords:
Buckling
Elastic shells
Mechanical instability
Oval shells
Inversion pathways
Interfacial friction

ABSTRACT

Curved elastic shells snap between two stable states, a feature widely used in soft actuators and deployable structures. Spherical shells are well understood, but how geometric orthotropy and the associated curvature distribution reshape their buckling and inversion remains unclear. Here we study oval shells under pressure-driven actuation, combining experiments and finite element simulations to examine how the aspect ratio, the supporting rim, and interfacial friction govern their response. A rimmed shell does not buckle in a single way as its aspect ratio increases but undergoes a transition in which the governing instability shifts from a rim-dominated mode, localized at the shell–rim junction, to a shell-dominated mode in the body. Strain-energy analysis reveals how the rim's prebuckling contribution differs between forward and reverse inversion, and Fourier analysis across aspect ratios, inversion pathways, and rim conditions clarifies the modal competition underlying buckling-mode selection in rimmed shells. The forward and reverse inversion pathways behave asymmetrically because the rim begins stress-free in one and pre-stressed in the other. Beyond buckling, self-contact and interfacial friction set the pressure for complete inversion, with friction raising it sharply and reshaping the path. These findings clarify how aspect-ratio-dependent curvature distribution, together with contact, governs shell inversion and suggest potential design implications for pressure-actuated shell-based soft machines.

1. Introduction

Bistable elastic shells can switch between distinct equilibrium configurations through geometrically nonlinear deformation. This behavior has been examined in natural systems such as Venus flytraps (Forterre et al., 2005; Volkov et al., 2007; Esser et al., 2020; Durak et al., 2022) and seed pods (Armon et al., 2011; Hofhuis et al., 2016; Hayashi et al., 2009; Bende et al., 2015), and has been used in engineered structures including energy harvesters (Cottone et al., 2009; Harne and Wang, 2013; Pellegrini et al., 2013; Stanton et al., 2009), deployable and morphing structures (Mallol et al., 2018; Pirrera et al., 2010; Seffen and Pellegrino, 1999; Norman et al., 2008), soft valves and actuators (Kim et al., 2025; Mosadegh et al., 2010; Choe et al., 2023; Tang et al., 2020; Chen et al., 2018), and architected mechanical metamaterials (Raney et al., 2016; Shi et al., 2021). In these systems, functional performance is governed not only by the existence of two stable configurations, but also by the instability pathway connecting them. In particular, the onset of buckling, the subsequent post-buckling evolution, and the completion of inversion determine the required inversion pressure, deformation symmetry, and repeatability of the transition (Gorissen et al., 2020; Qiao et al., 2021).

The mechanics of shell instability have been extensively studied for spherical caps and other axisymmetric shells. Previous work has clarified the roles of geometric nonlinearity, imperfection sensitivity, loading path, and material response in determining buckling and post-buckling behavior (Hutchinson and Koiter, 1970; Taffetani et al., 2018; Chen et al., 2012; Hutchinson, 1967; Hutchinson, 2016). Experimental and theoretical studies have further shown that shell transitions may depend strongly on loading rate, damping, and viscoelasticity (Gomez et al., 2017; Liu et al., 2023; Gomez et al., 2019), while recent studies have considered swelling, prestress, composite layups, and multi-material fabrication as means of programming bistable responses (Liu et al., 2023; Kim et al., 2012; Zhang et al., 2023; Boley et al., 2019; Xu et al., 2023). These studies provide a basis for understanding pressure-induced

* Corresponding authors.
E-mail addresses: annalee@postech.ac.kr (A. Lee), hajh@ajou.ac.kr (J. Ha).
[1] These authors contributed equally to this work.

https://doi.org/10.1016/j.ijsolstr.2026.114424
Received 13 July 2026; Received in revised form 16 October 2026; Accepted 27 October 2026
Available online 28 October 2026
0020-7683/© 2026 Elsevier Ltd. All rights are reserved, including those for text and data mining, AI training, and similar technologies.

inversion in shells. However, most previous studies have focused on spherical caps and other shells with relatively uniform curvature distributions. In oval shells, the curvature varies continuously along the perimeter, introducing directional variations in stiffness, buckling localization, and post-buckling evolution (Seffen, 2007; Shan et al., 2015; Pezzulla et al., 2018). Such geometric orthotropy can modify both the localization and propagation of deformation during shell inversion, yet how these effects govern the progression from buckling onset to inversion completion remains insufficiently understood.

Oval or elliptical shells introduce an additional geometric parameter, the aspect ratio, which sets their geometric orthotropy and curvature distribution. Oval and elliptical shells have long been studied in the context of pressure vessels, domes, and underwater pressure hulls, where egg-shaped geometries can outperform the classical spherical shell in load capacity and space efficiency (Zhang et al., 2017). These studies, however, treat full or clamped shells, regard buckling as a failure mode to be avoided, and involve geometries that are typically oblate or rimless. Shell inversion also occurs in living systems. The green alga Volvox turns its spherical embryo inside out during development, and in type A inversion the process begins at a single localized site, the phialopore, and propagates sequentially toward the opposite pole without self-contact (Höhn et al., 2015). A continuum description casts this as the flipping and peeling of elastic lips, in which bending, hoop stretching, and rotational resistance compete to produce bistability, with the intrinsic curvature acting as the control parameter (Haas and Goldstein, 2018). Inversion there is driven actively by cell shape changes rather than by external pressure, and the embryo carries no supporting rim, yet the observation that a localized instability dictates the entire transition pathway parallels what we find in rimmed oval shells. A separate line of work in soft robotics instead exploits the snap-through instability of rimmed hemispherical shells to build soft valves, pumps, grippers, and magnetically driven actuators, where the supporting rim is what makes bistability possible (Rothemund et al., 2018; Buranabunwong, 2024; Wen, 2025). Almost all of these devices remain confined to spherical geometry. How a rimmed prolate oval shell buckles and inverts under pressure, and how its aspect ratio reshapes that pathway, has not been established.

Studies on elliptical cylindrical shells have shown that aspect ratio can alter stability characteristics, imperfection sensitivity, and the transition between shell-like and plate-like responses under compression (Silvestre, 2008; Tvergaard, 1976; Boiko et al., 2009; Feinstein and Erickson, 1971; Arbocz and Babcock, 1969; Tennyson et al., 1971; Shariati and Mahdizadeh Rokhi, 2010; Vella et al., 2012). Bistable elliptical shallow shells have also been investigated in the context of orthotropic materials and prestressed configurations, where geometry and material anisotropy affect the existence and stability of multiple equilibria (Seffen, 2007; Guest and Pellegrino, 2006; Schenk and Guest, 2014; Vidoli and Maurini, 2008). In addition, elliptical geometries naturally interact with non-circular boundary constraints and asymmetric deformation pathways that frequently arise in practical shell systems (Sobota and Seffen, 2019). These studies indicate that the aspect ratio and the resulting curvature distribution can be used to tune shell deformation. Nevertheless, pressure-driven inversion of oval shells has not been systematically characterized in terms of the full deformation sequence. In particular, it remains unclear how aspect ratio controls the transition from buckling onset to inversion completion, and whether the dominant instability is governed by the shell body or by boundary structures such as a supporting rim.

Boundary and contact conditions add further complexity to shell inversion. In practical shell systems, the deformable shell is often connected to a supporting frame, bonded to a substrate, or brought into self-contact during large deformation. Contact mechanics and friction are known to modify deformation paths and energy dissipation in soft and thin structures (Pietrzak and Curnier, 1999; Barber and Ciavarella, 2000; Persson, 2001; Vakis et al., 2018; Kendall, 1975). For bistable shells, these effects are especially important because inversion often involves sliding, folding, and self-contact after the initial instability. Recent studies on shell eversion and contact-mediated snap-through have begun to show that contact constraints can substantially modify stability thresholds, contact states, and inversion pathways in bistable shells (Huang et al., 2024). However, quantitative experimental data on how interfacial friction modifies the pressure required for inversion completion remain limited, particularly for oval shells with varying aspect ratios.

Here, we investigate pressure-induced forward and reverse inversion of oval elastic shells using experiments and finite element simulations. We distinguish the initial localized instability from the subsequent completion of inversion. We define *buckling onset* as the first localized instability observed during pressure loading, and *inversion completion* as the final rapid transition associated with the completion of the forward or reverse inversion process. The terms *forward inversion* and *reverse inversion* denote the transitions from the natural to the everted configuration and from the everted to the natural configuration, respectively. Using silicone shells with controlled aspect ratios, we measure the pressure responses and deformation pathways under positive and negative pressure loading. We show that the supporting rim induces a transition between rim-dominated and shell-dominated buckling modes, with different critical aspect ratios for forward and reverse inversion. We further demonstrate that post-buckling deformation, self-contact, and interfacial friction govern the pressure required for inversion completion. Finite element simulations reproduce the observed deformation modes and provide insight into the role of geometry, boundary constraint, and contact in determining the inversion pathways of oval shells.

This paper is structured as follows. Section 2 introduces the problem formulation, parametric description, and morphological behaviors under positive and negative pressure regimes. Section 3 details the fabrication process, geometry control across varying aspect ratios, and characterization of shell material properties. Section 4 presents the experimental pressure responses under both non-lubricated and lubricated interface conditions. Sections 5 and 6 describe the numerical simulation framework and investigate the effect of aspect ratio on buckling pressures and mode changes. Section 7 combines strain-energy and Fourier modal analyses to characterize the pre-buckling contribution of the rim and the development of the selected instability branch. Section 8 then explores post-buckling behaviors, including the isolation of intrinsic elasticity and interfacial friction during forward and reverse complete inversion. Finally, Section 9 summarizes the key conclusions of this work.

2. Morphological study of oval shells

2.1. Experimental methods

Elastic shells with oval-shaped geometries are defined by distinct semi-axes along the x- and y-directions as shown in Fig. 1(a). We designate the semi-minor axis along the x-axis as R_x and the semi-major axis along the y-axis as R_y, both measured at the shell's mid-surface to ensure geometric consistency among samples. The shell thickness t is uniformly set to 300 μm, encompassing both the central dome and the brim-like extension surrounding it. A rigid acrylic ring supports the shell from below, positioned at a fixed radial distance τ from the outer boundary of the shell. This defines the outer boundary radius as $R_b = R_x + \tau$. To characterize the geometric orthotropy of the oval shell profile, we define the aspect ratio as $\mathrm{AR} = R_y/R_x$. Varying R_y while keeping R_x fixed changes the relative semi-axis lengths and, with them, the shell's local curvature distribution. In all experiments, $t = 300$ μm, $\tau = 1$ mm, and $R_x = 6$ mm are fixed to isolate the effect of aspect ratio on shell morphology and mechanical response.

Each shell specimen is mounted on an acrylic plate featuring a central circular aperture with a radius $R_b = 7$ mm, which serves as the outer boundary of the shell. The shell is carefully aligned with the center of the

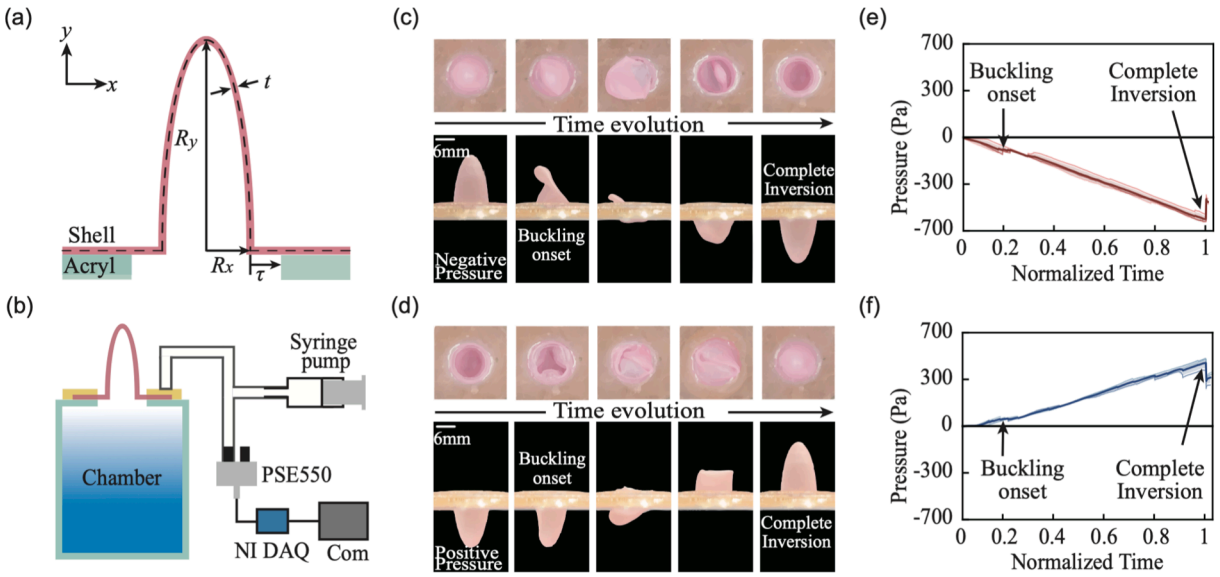

Fig. 1. Geometry, experimental setup, and pressure-driven inversion of an oval shell. (a) Cross-sectional geometry of the shell, defined by the **semi-minor axis** R_x, the **semi-major axis** R_y, the wall thickness t, and the rim width τ. (b) Pressure-driven test setup, in which a syringe pump sets the chamber pressure while a pressure sensor and a data-acquisition unit record it. (c) Forward inversion under decreasing (negative) pressure, shown in top and side views from the onset of buckling to complete inversion (scale bar, 6 mm). (d) Reverse inversion of the same shell under increasing (positive) pressure. (e, f) Chamber pressure versus normalized time for the (e) forward (red) and (f) reverse (blue) processes, where the solid line denotes the mean, the shaded band ± 1 SD, and the sharp pressure drop and recovery mark the buckling and **complete inversion** events.

aperture to minimize geometric eccentricity. A thin layer of polyurethane adhesive (Vyta Flex 20, Smooth-On, Inc.) is applied around the perimeter of the shell to fix it onto the plate, avoiding any seepage into the inner region. To ensure airtight conditions during pressure loading, all interfaces between the acrylic plate and the surrounding chamber are sealed using silicone. The shell–plate assembly is connected to a 30 mL syringe pump (KDS-100, KD Scientific) via flexible tubing and equipped with a differential pressure sensor (SMC PSE550, SMC). The sensor is interfaced with a data acquisition module (NI USB-6003, National Instruments, USA), which records the pressure data through a LabVIEW-based acquisition system. Prior to experimentation, the pressure sensor is calibrated to convert voltage outputs into absolute pressure values. The overall experimental setup, including the shell mounting, sealing, and pressure-sensing components, is illustrated in Fig. 1(b).

During testing, the syringe pump imposes a constant volumetric flow rate of 50 μL/min, generating either positive or negative pressure depending on the flow direction. This loading induces gradual deformation of the shell structure, ultimately leading to buckling and inversion transitions. A preliminary reverse inversion test is performed prior to each main trial to precondition the shell. This preconditioning is necessary because silicone elastomers exhibit pronounced first-cycle stress softening. An initial loading cycle stabilizes the deformation behavior and ensures that the measured instability pressures reflect a steady, repeatable mechanical response. For each baseline experimental condition at 50 μL/min, three independent shell specimens are tested. The average critical pressure and corresponding standard deviation are calculated from all measurements. To test whether 50 μL/min is slow enough for quasi-static loading, we additionally measure the complete-inversion pressures at 100 and 200 μL/min for non-lubricated shells with AR = 1 and 5 and lubricated shells with AR = 5. Delayed instability and viscoelastic stiffening can raise the measured pressures at faster loading (Gomez et al., 2017; Liu et al., 2023; Gomez et al., 2019), but the complete-inversion pressures at these higher flow rates show no systematic increase relative to those at 50 μL/min (Supplementary Section S1 and Table S1). The time scales of the experiment lead to the same conclusion. At 50 μL/min, the stage from buckling onset to complete inversion alone lasts approximately 6–60 s, whereas the elastic response time of the shells and the stress-relaxation time reported for a silicone elastomer are about 1 s or shorter (Supplementary Section S1). We therefore treat the loading at 50 μL/min as a quasi-static approximation for the measured complete-inversion pressures, although the snap-through events themselves remain dynamic.

2.2. *Pressure-induced inversion and buckling instability*

Shell inversion under pressure loading proceeds through mechanically distinct stages characterized by gradual deformation followed by abrupt geometric reconfiguration. We distinguish between two inversion processes based on the direction of pressure loading and the initial configuration of the shell: forward inversion, in which the shell transitions from its as-molded configuration to an everted state under negative pressure [see Fig. 1(c)], and reverse inversion, in which the everted shell returns to its original configuration under positive pressure [see Fig. 1(d)]. A shell with an aspect ratio of three (AR = 3) serves as a representative example, as it exhibits clear transitions in both processes.

Under negative pressure, the shell initially undergoes axisymmetric compression as air is gradually withdrawn from the chamber. As the pressure magnitude increases, the shell reaches a critical point where it loses axisymmetric stability and begins to buckle, as shown in Fig. 1(c). This buckling instability manifests as localized dimpling or wrinkling near the rim-shell junction. Following buckling, the shell undergoes forward inversion, during which the geometry transitions abruptly from a positive curvature configuration to a fully everted state with negative curvature. This transition is accompanied by a sudden pressure change, reflecting the release of elastic energy stored during the pre-buckling deformation. The corresponding pressure response is shown in Fig. 1(e), where the internal pressure is plotted against normalized time, defined as the ratio between the elapsed time t and the characteristic complete inversion time t_s (i.e., t/t_s). The characteristic time t_s corresponds to the instant at which the peak pressure associated with the complete inversion event occurs, so that the complete inversion event occurs at $t/t_s = 1$ for all cases. The complete inversion time t_s is chosen as the characteristic time because it represents the dominant instability event governing the shell transition, and normalizing the time axis by t_s allows direct comparison of pressure evolution across shells with different aspect ratios and deformation durations. In Fig. 1(e), the onset

of buckling appears as a subtle plateau or inflection in the pressure curve, followed by a sharp drop marking the complete inversion point.

Under positive pressure, the everted shell follows a qualitatively similar but quantitatively distinct pathway, as shown in Fig. 1(d). Air injection increases the internal pressure, causing the everted shell to expand outward. At a critical pressure, the shell again buckles near the rim-shell junction, initiating the reverse inversion. The shell then returns to its original configuration through a sudden transition that follows the reverse geometric path. The corresponding pressure response is shown in Fig. 1(f), again plotted against normalized time. Here, buckling appears as a deviation in slope, and the complete inversion is indicated by a pronounced pressure peak before a rapid release. In both processes, small oscillations are often observed between the buckling and complete inversion points, likely associated with stick–slip interactions caused by interfacial friction during shell deformation. Notably, the forward inversion pressure consistently exceeds the reverse inversion pressure. This asymmetry originates from the manufacturing bias of the shell, which is molded in its undeformed configuration, making the return to the original state energetically more favorable than the initial inversion.

3. Fabrication and characteristics of oval shells

3.1. Shell molding and geometry control

Oval-shaped shells are produced using a molding process illustrated in Fig. 2(a). The mold consists of a two-part structure fabricated using a 3D printer (Form 4, Formlabs), featuring dedicated inlet and outlet channels that guide the flow of silicone into the central cavity while releasing excess material. A syringe is used to inject the silicone into the mold cavity under an applied pressure of approximately 100–200 kPa. As the silicone fills the cavity, air is expelled through the outlet, and once fully filled, the mold is left undisturbed for curing. Two types of silicone, Elite Double 8 and Ecoflex 00–30, are employed as the shell materials. After curing, the shell is gently demolded. To facilitate this process for shells with high aspect ratios, especially those with aspect ratios greater than three, a small vent hole is incorporated at the base of the mold to introduce air during release. Once demolded, excess material near the vent is trimmed using fine tweezers and a scalpel. Each molded shell is then adhered onto a rigid chamber using polyurethane adhesive, completing the assembly for mechanical testing, as shown in the final stage of Fig. 2(a).

A series of oval-shaped shells with varying aspect ratios from AR = 1 to 5 are fabricated from Elite Double 8 silicone using this method, as displayed in Fig. 2(b). All shells are molded with a fixed semi-minor axis of 6 mm, while the semi-major axis is systematically increased to control the aspect ratio. As the aspect ratio increases, the shell geometry evolves from a hemispherical dome to a progressively more elongated profile. To verify the uniformity and consistency of the molded shells, we conduct cross-sectional image analysis of the shell wall thickness. Each shell is bisected through its vertical midplane, and thickness measurements are performed at thirty-seven locations distributed symmetrically from the apex to the rim of the shell. The resulting data are presented in Fig. 2(c), which shows the mean and standard deviation of thickness across five specimens per aspect ratio. The results confirm that the shell wall remains approximately constant near the target thickness of 300 μm throughout the entire profile, indicating a high degree of precision and reproducibility in the molding process.

3.2. Mechanical properties of shell materials

To quantify the elastic properties of the materials used in shell fabrication, we perform uniaxial tensile tests on molded dog-bone specimens, as illustrated in Fig. 2(d). Each specimen features a gauge section 6 mm wide, 32 mm long, and 4 mm thick, with tapered shoulders to minimize stress concentrations during loading. As shown in the inset of Fig. 2(d), the samples are mounted vertically on a universal testing machine (Instron 3343, Instron Corp., USA) and subjected to monotonic tension under displacement-controlled conditions. The specimens are tested in accordance with the ASTM D412 standard. The total strain is limited to approximately 60%. All tests are conducted under ambient temperature and humidity.

We extract the Young's modulus from a linear fit within the strain range of 0.02–0.05, which excludes the toe region often affected by grip settling and captures the intrinsic elastic response of the material. This range defines only the initial modulus and does not limit the strain in the simulations, which use the finite-strain Neo-Hookean model described in Section 5. The resulting stress–strain curves are plotted in Fig. 2(e), showing the averaged mechanical response from five repeated tests per material. In this elastic regime, Elite Double 8 demonstrates a steeper slope, corresponding to a higher Young's modulus of approximately 227 kPa, while Ecoflex 00–30 shows a softer response with a modulus of

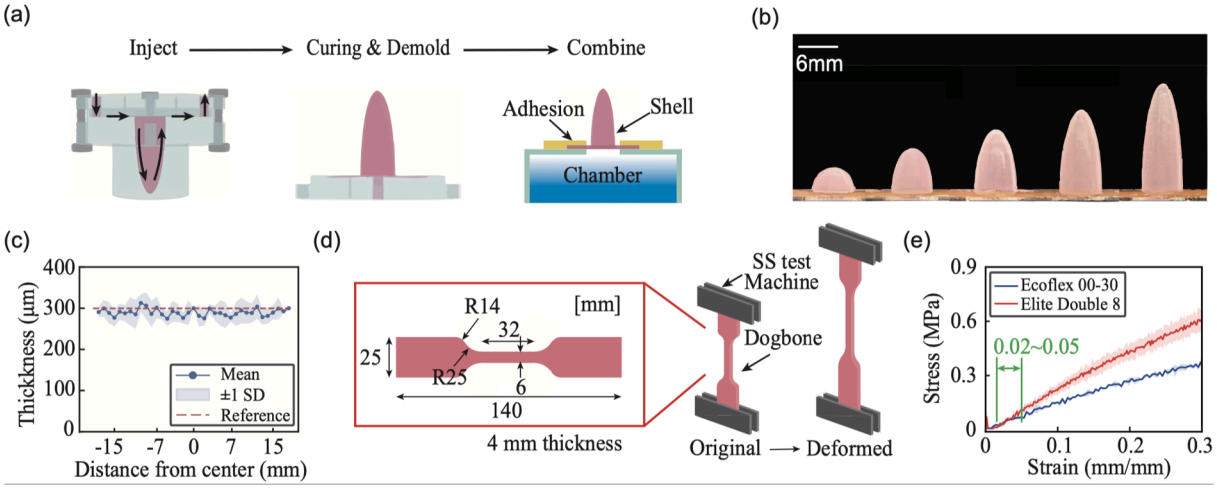

Fig. 2. Fabrication and material characterization of oval shells. (a) Fabrication sequence, in which silicone is injected into a mold, cured and demolded, and then bonded to the pressure chamber. (b) Photographs of fabricated shells spanning aspect ratios from 1 to 5 (scale bar, 6 mm). (c) Measured wall thickness along the meridian, confirming a nearly uniform thickness of about 300 μm, where blue circles denote the mean, the shaded band ± 1 SD, and the red dashed line the reference thickness. (d) Dog-bone specimen and the uniaxial tensile test used to measure the material response. (e) Stress–strain curves of Elite Double 8 (red) and Ecoflex 00–30 (blue), where the solid line denotes the mean, the shaded band ± 1 SD, and the green arrows mark the low-strain linear range (0.02–0.05) used to extract the modulus.

about 122 kPa. The shaded bands represent the standard deviation across the five specimens, confirming a high level of repeatability in both material preparation and testing.

We assume a Poisson's ratio of 0.5 for both materials, consistent with the nearly incompressible nature of silicone-based elastomers. These experimentally obtained moduli are used as input parameters for analytical predictions and finite element simulations of shell deformation under pressure loading. The mechanical contrast between the two silicones is later reflected in their distinct buckling and inversion responses, with the softer Ecoflex material exhibiting lower critical pressures and more compliant deformation profiles.

To examine the effects of shell geometry, the supporting rim, and contact on the elastic buckling and inversion response, we adopt a rate-independent hyperelastic model. This provides an elastic reference for interpreting the observed deformation pathways and pressure trends. Viscoelastic relaxation and dissipation, which can influence the time-dependent response of silicone domes (Brinkmeyer et al., 2012), are beyond the present constitutive description. Incorporating these effects through material-specific characterization and viscoelastic modeling represents an important direction for future refinement.

4. Experimental results

4.1. Pressure responses under non-lubricated conditions

The pressure responses plotted against normalized time reveal the critical transitions of buckling and inversion in oval shells under pressure loading, as shown in Fig. 3(a–d). The left panels (a, b) capture forward inversion under vacuum (negative pressure), where the shell snaps from its original geometry into the everted state, while the right panels (c, d) capture reverse inversion under pressurization (positive pressure), where the shell snaps back to its original configuration. Each pressure regime is examined for two silicone elastomers of differing stiffness, Elite Double 8 (a, c) and Ecoflex 00–30 (b, d), allowing the material dependence of the instability to be compared within each inversion mode. For each baseline condition at 50 μL/min, the reported pressures are based on three independent shell specimens. The plotted means and standard deviations indicate the variability among these specimens.

During forward inversion, air is withdrawn from the chamber so that the internal pressure decreases until the shell loses its axisymmetric shape, marking the onset of buckling [open triangles in Fig. 3(a, b)]. Continued evacuation produces a rapid geometric inversion accompanied by a sudden pressure drop, the complete inversion event (filled triangles). The two materials follow the same qualitative sequence but differ markedly in magnitude. The complete inversion pressures of Ecoflex 00–30 [Fig. 3(b)] remain consistently lower than those of Elite Double 8 [Fig. 3(a)] across all aspect ratios. This contrast originates in the lower Young's modulus of Ecoflex, which reduces the shell stiffness and lowers the mechanical barrier to instability, so the softer material accommodates more compliant deformation and reaches the critical pressures for buckling and complete inversion at smaller magnitudes.

During reverse inversion, the pressure rises from the everted state so that the shells expand until they reach a local instability at the buckling point [open triangles in Fig. 3(c, d)], followed by recovery to the original configuration (filled triangles). These reverse transitions consistently occur at lower pressure magnitudes than their forward counterparts, reflecting the energetic bias of the system: the shells are molded in their original, non-everted shapes, so returning to that configuration demands less energy than forcing the shell into inversion. The material contrast persists in this mode as well, with Ecoflex 00–30 [Fig. 3(d)] recovering at lower pressures than Elite Double 8 [Fig. 3(c)], again consistent with its lower stiffness and reduced resistance to deformation.

Minor oscillations between the buckling and complete inversion points appear across various cases in Fig. 3. These fluctuations likely arise from stick–slip interactions associated with internal friction or intermittent self-contact during deformation. The effects become significantly less pronounced under lubricated conditions (Section 4.2), supporting the interpretation that interfacial friction contributes to the observed pressure oscillations.

4.2. Pressure responses under lubricated conditions

Interfacial friction at the shell–substrate and shell–shell contacts acts as a stabilizing mechanism that raises the instability thresholds of the oval shells. In the non-lubricated state, tangential drag at these interfaces anchors the shell and resists relative sliding, so higher pressures are needed to overcome both the elastic restoring forces and the frictional resistance. This anchoring effect grows more pronounced at larger aspect ratios, which demand greater lateral displacement and more extensive self-contact. Because friction superimposes on the intrinsic elastic instability, it obscures the true material- and geometry-dependent response of the shells. Resolving this intrinsic behavior, therefore, motivates a controlled reduction of interfacial friction, which we achieve through surface lubrication.

We reduce friction by coating both the inner and outer contact regions of the shell with a thin film of talcum powder (Baby Powder, Johnson & Johnson), applied with a brush over the areas where the shell interfaces with the supporting chamber [Fig. 4(a)]. This layer substantially reduces interfacial resistance and facilitates relative sliding during deformation, while retaining a finite effective friction coefficient. Optical microscopy of the contact interface confirms the coating. The untreated silicone shows a micro-texture inherent to the molding process [Fig. 4(a–I)], whereas after treatment, the talcum particles fill the surface asperities and form a continuous lubricating layer at the 200 μm scale [Fig. 4(a–II)], shifting the contact from high-friction polymer-on-polymer interaction to a mediated sliding interface. We quantify the resulting friction with a commercial tribometer (MCR 302e, Anton Paar) at room temperature (25 °C), sliding the upper specimen at 0.01 m/s under normal loads of 0.2 N, 0.5 N, and 1 N, with a 3 min equilibration

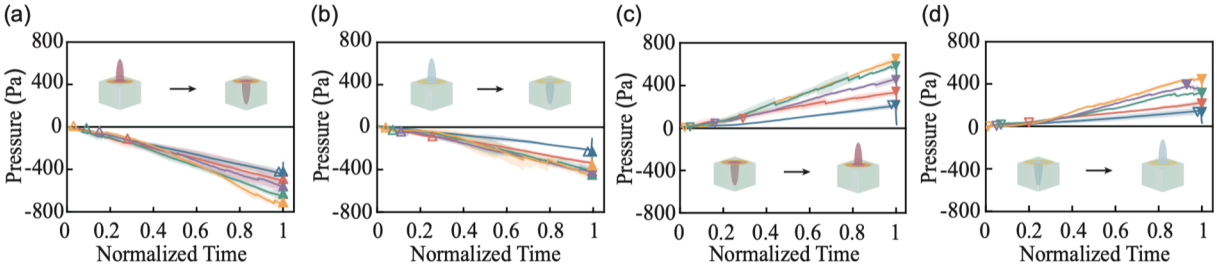

Fig. 3. Buckling and inversion transitions of non-lubricated oval shells. (a, b) Chamber pressure versus normalized time during forward inversion under decreasing pressure for (a) Elite Double 8 and (b) Ecoflex 00–30, where open symbols mark the buckling onset and filled symbols mark the complete inversion event. (c, d) The corresponding reverse inversion under increasing pressure for (c) Elite Double 8 and (d) Ecoflex 00–30. The insets illustrate the shape change in each process, and each panel collects shells of different aspect ratios to show how the transition pressures shift with geometry. The line color denotes the aspect ratio (blue, red, purple, green, and orange for AR = 1, 2, 3, 4, and 5, respectively), and the shaded bands denote ± 1 SD.

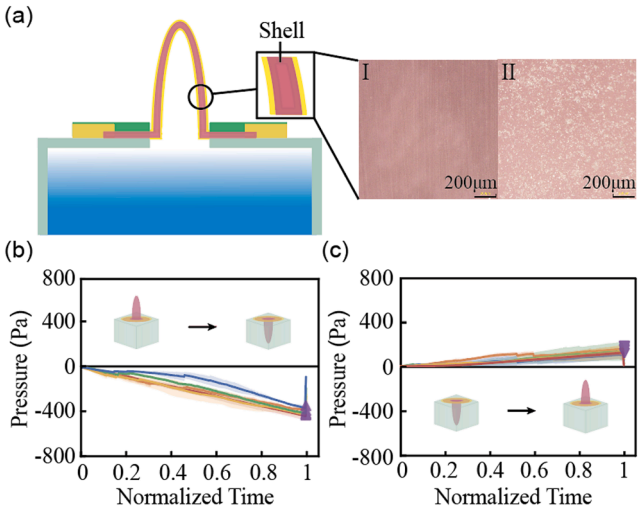

Fig. 4. Effect of lubrication on the inversion of oval shells. (a) Lubrication strategy, in which a thin talcum-powder layer (yellow) coats the contact surfaces to minimize interfacial friction, with optical micrographs of the silicone surface (I) before and (II) after treatment (scale bar, 200 μm). (b, c) Chamber pressure versus normalized time under lubricated conditions during the (b) forward and (c) reverse processes, showing markedly lower complete inversion pressures than the non-lubricated shells in Fig. 3. The line colors and symbols follow the same conventions as in Fig. 3.

and 50 s of continuous recording for each load. Averaging the load-specific steady-state values with equal weighting yields an effective friction coefficient of 0.545 ± 0.031, well below the near-unity values typical of dry soft silicone elastomers (Shore A8) (Berthold et al., 2023), which confirms the reduced surface adhesion and improved interfacial slip.

Fig. 4(b) presents the pressure responses against normalized time during the forward inversion under lubricated conditions, and Fig. 4(c) presents the corresponding reverse inversion. Because the lubricated and non-lubricated experiments are measured separately, the effect of lubrication emerges from a direct comparison with the non-lubricated responses in Fig. 3(a, c), which shows that the lubricated complete inversion pressure falls well below the non-lubricated values for both processes. More importantly, the lubricated complete inversion pressures depend only weakly on aspect ratio, whereas the non-lubricated case remains strongly sensitive to geometry. This difference indicates that interfacial friction not only raises the absolute complete inversion pressures but also amplifies the influence of shell geometry on the instability thresholds. Once friction is minimized, the reduced tangential resistance at both interfaces lets the shell rotate and slide with little constraint, accommodating the large deformations required for inversion. These observations identify interfacial friction as the dominant source of the elevated, geometry-sensitive complete inversion pressures in the non-lubricated shells.

5. Numerical simulation

We perform finite element simulations of the inversion behavior of oval shells across various aspect ratios in a commercial package, ABAQUS/STANDARD. We model every oval shell as an incompressible hyperelastic material using a three-dimensional Neo-Hookean formulation. Based on the material testing results for Elite Double 8 and the pressure loading experiments, we set the shear modulus to $\mu = 0.07586$ MPa (i.e., $C_{10} = 0.03793$ MPa), and the compressibility parameter to $D = 0$ to enforce incompressibility. The geometry follows Fig. 1(a), and we model the clamping ring by extending the geometry to a radial distance of $\tau = 1$ mm, with a pinned boundary condition on the lateral surface at the end of the ring. We discretize the full 3D shell with 8-node reduced hybrid elements (C3D8RH) and 6-node hybrid elements (C3D6H), using a hex-dominated sweep of five elements through the thickness and a minimum of 60 elements in the azimuthal and meridional direction. We mesh the ring with a structured hexahedral grid of five elements in the radial direction.

Following the classical derivation by Zoelly (Zoelly, 1915), the critical buckling pressure of a spherical shell can be predicted as

$$P_c = \frac{2E}{\sqrt{3(1-\nu^2)}}\left(\frac{t}{R_x}\right)^2 \tag{1}$$

where E is the Young's modulus, ν is the Poisson's ratio, and R_x and t are the semi-minor axis and thickness, respectively. The value of P_c follows from the material and geometry of the experiments. The classical Zoelly pressure P_c in Eq. (1) is used here as a reference pressure for normalizing the buckling pressure and defining the characteristic load scale in the simulations.

To investigate the nonlinear response, both static Riks analysis and dynamic implicit analysis were employed, with each approach serving a distinct purpose depending on the deformation regime. The initial buckling behavior was rigorously characterized using a static Riks step (arc-length method), which enables accurate tracing of equilibrium paths under geometric nonlinearity. This approach provides reliable predictions of buckling pressure and corresponding mode shapes under quasi-static conditions. In contrast, the post-buckling regime involves extremely large deformations accompanied by extensive contact interactions, which pose significant challenges in achieving stable solutions under static conditions or strictly quasi-static conditions. In particular, enforcing sufficiently slow loading rates to fully suppress dynamic effects leads to high computational cost due to severe time increment refinement. Therefore, a dynamic implicit analysis with a finite step time was adopted to capture the overall inversion behavior in a computationally efficient manner.

In each dynamic implicit step, the applied pressure is increased linearly from zero to its prescribed maximum over the step time T, so a longer step time corresponds to a lower loading rate. To select an appropriate finite step time for the dynamic implicit analyses, we perform a step-time sensitivity study for forward inversion of the representative high-aspect-ratio shell ($AR = 3$) using $T = 1$, 10, 20, 100, and 1000. The normalized complete-inversion pressure progressively approaches a plateau as the step time increases [Supplementary Fig. S1 (a, b)]. For this $AR = 3$ forward case, the predicted pressure at $T = 10$ is 6.15% higher than the $T = 1000$ value [Supplementary Fig. S1(b)]. For $T \geq 10$, the sustained background level of the ratio of kinetic to internal energy reported by ABAQUS (ALLKE/ALLIE) is substantially lower than in the $T = 1$ calculation [Supplementary Fig. S1(c)]. Based on this

balance between reduced loading-rate dependence and computational cost, we adopt $T = 10$ for the quantitative analysis of the complete-inversion pressure.

For the forward inversion process analysis, the buckling pressure was determined from the static Riks step by applying a uniform pressure up to $-P_c$ on the inner surface of the structure and identifying the first local maximum of the pole displacement-normalized pressure curve. The complete inversion pressure was obtained from the dynamic step by applying a uniform pressure approximately $-1.7P_c$, a value consistent with experimental results and suitable for ensuring numerical convergence, and identifying the point at which the pole displacement–normalized pressure curve exhibits a peak. For the reverse inversion process analysis, the shell was analyzed under applied pressure in its everted configuration. To prepare the everted shell, two preliminary steps were performed: the shell was first subjected to forward inversion under a dynamic step, followed by a load-free static general step to bring the everted configuration into nearly complete equilibrium. The buckling and complete inversion pressures during reverse inversion were then determined in the same manner as in the forward inversion process, using $+P_c$ and $+1.7P_c$, respectively. All analyses were performed with geometric nonlinearity activated, and the quasi-static application option in ABAQUS was employed throughout the dynamic implicit analysis.

A mesh convergence study for the Riks analysis is conducted over approximately 10 k to 80 k elements, demonstrating robust convergence beyond 40 k elements, with variations within ~ 2%. For the dynamic step analysis, simulations are primarily performed using meshes with more than 40 k elements, which show good convergence behavior in the Riks analysis. For AR = 4 and 5, however, meshes with approximately 20 k elements are employed, considering the computational cost, as they still provide reasonably converged results with variations within ~ 5%. Supplementary Video S1 compares the experimental and simulated morphological evolution of shells with AR = 1–5 during forward and reverse inversion. The simulations in Supplementary Video S1 and the simulated configurations discussed in Section 8 were obtained with a step time of $T = 1$ and are retained as qualitative illustrations of deformation and contact. They provide clearer fixed-viewpoint sequences of the same major events, without the additional azimuthal reorientation observed at $T = 10$ for the representative AR = 3 shell. The simulated pressure results in Section 8 use $T = 10$.

We omit explicit geometric imperfections from the nominally perfect reference calculations so that the selected mode is not biased toward the shape of an imposed imperfection. Small non-axisymmetric components arising from the discretization and the numerical solution initiate departure from the axisymmetric path, and their subsequent growth is examined through the Fourier decomposition described in Supplementary Section S3. To assess the numerical robustness of the mode-selection trends underlying the nominally perfect-shell buckling results in Sections 6 and 7, we analyze this growth during forward and reverse buckling of rimmed shells and forward buckling of rimless shells (Supplementary Fig. S2). We also repeat buckling calculations near the modal transition using alternative circumferential meshes. The Fourier histories identify the principal competing modes and distinguish their sustained growth from intermittent, mesh-sensitive excursions of weaker components. The same overall aspect-ratio-dependent pattern of modal competition and mode selection persists across the tested meshes, supporting the reproducibility of the reported forward modal transition in the nominally perfect calculations (Supplementary Fig. S3). The mesh comparison addresses the forward modal transition and does not quantify the sensitivity to fabrication imperfections of finite amplitude. The procedures, calculated buckling-pressure comparisons, and modal growth histories are provided in Supplementary Sections S3 and S4.

6. Effect of aspect ratio on buckling pressure and buckling modes

Following the well-established buckling behavior of spherical shells, we normalize the buckling pressures obtained from the various methods by the critical buckling pressure, P_c. Fig. 5(a) and (b) plot the normalized buckling pressure against aspect ratio for the forward and reverse inversion processes, comparing the numerical simulation results for shells with a rim (rimmed shells, black solid line) and shells without a rim (rimless shells, cyan solid line) together with the experimental data. In both processes, the buckling pressure decreases overall as the aspect ratio increases, while the rimmed curves change slope around the modal transition, at AR = 1.7 for the forward and AR = 2.4 for the reverse process. This change of slope reflects a handover in what controls the instability. At low aspect ratios, the shell is nearly hemispherical and intrinsically stiff, so the instability is triggered by the pressurized rim at the shell–rim junction. As the aspect ratio increases, the shell becomes progressively more slender and structurally less stable, so its buckling pressure decreases. Beyond the critical aspect ratio, buckling becomes shell-dominated and the rimmed and rimless predictions approach one another. The rimless shells (cyan) carry no rim contribution and therefore decrease smoothly and monotonically, lying above the rimmed curves at low aspect ratio and converging with them once buckling becomes shell-dominated. The forward and reverse processes differ in their critical aspect ratio because they start from different states of the shell and rim, namely the stress-free natural state and the pre-stressed everted state.

The insets in Fig. 5(a) and (b) highlight where buckling first sets in. Each inset pairs an experimental snapshot, with a red arrow marking the site of incipient buckling, with the corresponding numerical displacement field for the AR = 2 shell. Because this specific aspect ratio lies above the critical threshold for the forward inversion process ($AR_c = 1.7$) but below that for the reverse inversion process ($AR_c = 2.4$), it exhibits distinctly different instability modes depending on the inversion pathway. During forward inversion [inset of Fig. 5(a)], the instability occurs near the central region of the shell, representing a shell-dominated buckling mode. Conversely, during reverse inversion [inset of Fig. 5(b)], the instability localizes heavily near the shell–rim junction, characteristic of a rim-dominated buckling mode. The close agreement between the experimental observations and numerical simulations clearly corroborates how the shift relative to AR_c governs these dominant instability modes.

Removing the rim entirely isolates its role, and Fig. 5(c) shows the resulting buckling modes of rimless shells. In the absence of a rim, the deformation always localizes in the central region of the shell surface, away from the boundary, and this mode persists essentially unchanged across the aspect ratio range. No junction-localized mode appears, which confirms that the rim-dominated buckling seen in the rimmed shells originates entirely from the rim. Without a rim, the shell boundary imposes the same condition in both configurations, so the everted state is geometrically the mirror image of the natural state, and the two inversion directions are mechanically equivalent. The reverse inversion path, therefore, coincides with the forward path for these shells, and we present only the forward case in Fig. 5(c). The displacement magnitudes are also much smaller than in the rimmed shells, consistent with the rim acting as the dominant source of localized deformation.

For the rimmed shells, Fig. 5(d) and (e) follow how the buckling mode evolves as the aspect ratio increases, for the forward (d) and reverse (e) processes. At low aspect ratios, the displacement concentrates near the shell–rim junction, giving a rim-dominated mode, while beyond the critical aspect ratio it migrates to the central region of the shell, giving a shell-dominated mode that resembles the rimless case in Fig. 5(c). This transition occurs near AR = 1.7 for the forward process and AR = 2.4 for the reverse process, the same aspect ratios at which the buckling pressure slope changes in Fig. 5(a) and (b). The shift arises because the pressure loading also pressurizes the rim. At low aspect

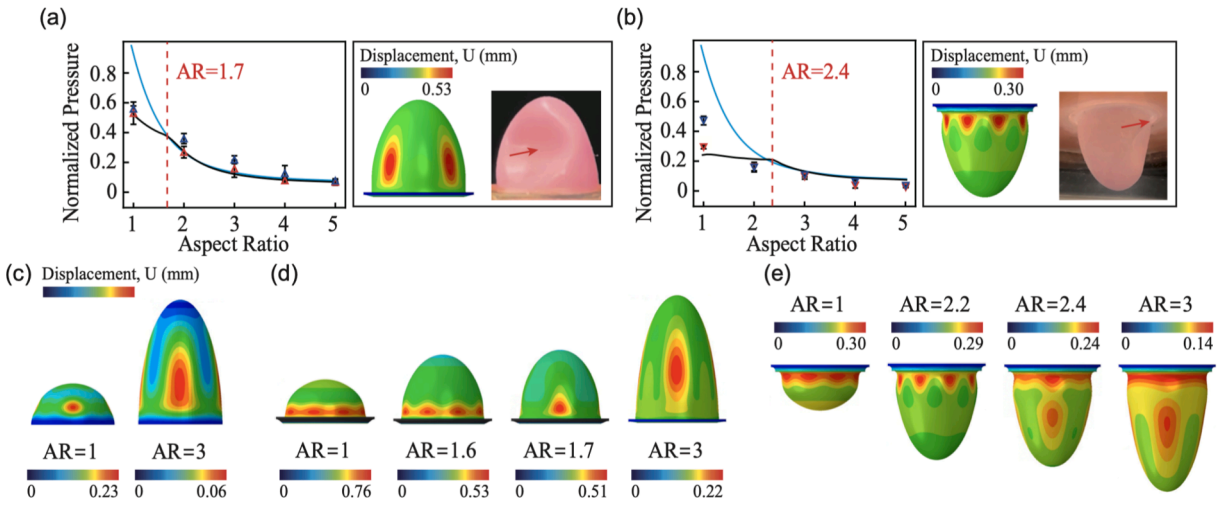

Fig. 5. Effect of aspect ratio on the buckling pressure and buckling modes. (a, b) Normalized buckling pressure versus aspect ratio for the (a) forward and (b) reverse processes, comparing shells with a rim (black) and without a rim (cyan) together with the experimental data (symbols, mean ± 1 SD), where the red dashed line marks the critical aspect ratio. Insets show an experimental snapshot, with the red arrow marking the site of incipient buckling, and the simulated displacement field at AR = 2. (c) Buckling modes of rimless shells during forward inversion at AR = 1 and 3, which stay centered on the shell regardless of aspect ratio. (d, e) Buckling modes of rimmed shells, showing the shift from a junction-localized (rim-dominated) mode to a shell-centered (shell-dominated) mode with increasing aspect ratio during the (d) forward and (e) reverse processes. Color denotes the displacement magnitude in millimeters.

ratios, the stiff shell resists buckling while the rim deforms substantially, so the added bending at the junction triggers a rim-dominated instability, whereas at high aspect ratios, the slender shell reaches its own instability first and buckles at its center before the rim can accumulate significant deformation. The progressively smaller junction displacement with increasing aspect ratio in Fig. 5(d) reflects this diminishing rim contribution.

7. Strain energy and modal analyses of the rim effect

The buckling pressure trends and deformation fields in Fig. 5 reveal a progressive transition from rim-dominated to shell-dominated instability as the aspect ratio increases. To characterize the underlying mechanics, we employ two complementary measures. The strain energy density (SENER) immediately before buckling, shown in Fig. 6, visualizes the pre-buckling loading introduced by rim deflection and its variation with aspect ratio. A circumferential Fourier decomposition of the non-axisymmetric normal displacement separately characterizes the instability branch that develops as buckling is approached. The detailed Fourier methodology and modal-amplitude histories are provided in Supplementary Section S3 and Supplementary Fig. S2.

During the forward inversion process, Fig. 6(a) plots the maximum SENER at the shell–rim junction as a function of aspect ratio. The junction energy density decreases monotonically, from about 1.2×10^{-3} MPa at AR = 1 to roughly 1.6×10^{-5} MPa at AR = 5. This progressive decrease stems from the interplay between intrinsic shell stability and rim deformation. Because the forward inversion begins from a stress-free state, the junction energy must be actively built up through rim deflection. However, as the aspect ratio increases, the shell becomes more slender and its intrinsic buckling resistance drops. Consequently, instability is triggered at increasingly lower pressures, leaving the rim with insufficient opportunity to bend and accumulate large strain energy. This steadily diminishing energetic contribution from the rim may be associated with the gradual decline in forward buckling pressure below the critical aspect ratio [Fig. 5(a)]. A separate pole curve is omitted for the forward process because the pole energy density, although not exactly zero, stays two to three orders of magnitude below the junction value at every aspect ratio, of order 10^{-5} MPa at AR = 1 and 10^{-8} MPa at AR = 5 against 10^{-3} to 10^{-5} MPa at the junction. Although the junction therefore remains the largest local SENER maximum, its magnitude is interpreted as a measure of the pre-buckling loading imposed by the rim. The selected non-axisymmetric instability branch is characterized separately using the Fourier amplitudes discussed below.

Mapping the full SENER fields just before buckling, Fig. 6(b) compares rimless (green-box) and rimmed shells at AR = 1 and AR = 5 in the forward process. For AR = 1, at the same applied pressure ($P/P_c \approx 0.53$, corresponding to the buckling onset of the rimmed shell), the rimless shell stores its energy broadly over the surface with a maximum of only 8.3×10^{-5} MPa and remains stable, whereas the rimmed shell concentrates energy sharply at the junction and reaches 1.2×10^{-3} MPa. This approximately 14-fold difference shows that the junction energy comes from the compatibility deformation imposed by rim deflection rather than from direct pressurization of the shell body. Because the natural shell carries no pre-stress, its strain energy grows from zero as the pressure rises, and the rim then deflects vertically downward, so the shell must change its curvature at the junction to stay compatible with the deflected rim. This compatibility-driven curvature change stores far more energy at the junction than the direct pressurization of the rest of the shell, which accounts for the pronounced junction-energy concentration in Fig. 6(b). For AR = 5, buckling is triggered at a nearly identical applied pressure ($P/P_c \approx 0.08$). Both maxima are far lower, 1.6×10^{-5} MPa with a rim and 3.0×10^{-6} MPa without, and the rimmed maximum exceeds the rimless one by only about a factor of five, consistent with the reduction in rim-induced pre-buckling loading as the shell elongates. Because a rimless shell has no rim to break the symmetry between its two configurations, its everted state is the mirror image of its natural state, so the forward and reverse processes are mechanically identical. The green-boxed rimless results, therefore, represent both inversion directions, and we show only the forward case.

Reverse inversion behaves very differently, as Fig. 6(c) shows. The junction energy density (red) stays nearly constant at about 3.5×10^{-3} MPa across the whole aspect ratio range, while the pole energy density (green) climbs steadily from the order of 10^{-3} MPa to about 2.5×10^{-2} MPa, overtaking the junction near AR ≈ 2. The contrast with the forward process is physical. Reverse inversion starts from a highly pre-stressed everted configuration, so the junction carries a persistent energetic hotspot set by the eversion pre-stress that barely depends on aspect ratio, which produces the constant red curve. Staying compatible with the everted rim at the junction forces the everted shell into an inward, integral-shaped curvature, so the whole shell is pushed radially inward

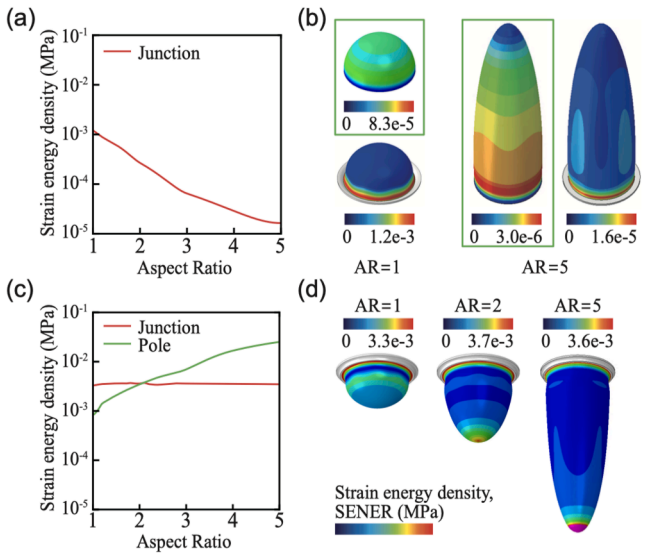

Fig. 6. Strain energy density (SENER) analysis of the rim effect. (a) Maximum SENER at the shell–rim junction (red) versus aspect ratio during forward inversion, which decreases monotonically as the shell elongates. (b) SENER distributions during forward inversion, comparing shells without a rim (green boxes) and with a rim at AR = 1 ($\mathbf{P/P_c \approx 0.53}$) and AR = 5 ($\mathbf{P/P_c \approx 0.08}$). (c) Maximum SENER at the junction (red) and at the pole (green) versus aspect ratio during reverse inversion, which cross near AR = 2. (d) SENER distributions just before buckling during reverse inversion at increasing aspect ratio (the purple spot at the AR = 5 pole denotes SENER between $3.63 \times \mathbf{10^{-3}}$ and $2.5 \times \mathbf{10^{-2}}$ **MPa**, exceeding the contour bounds). Color denotes the strain energy density in MPa.

relative to its natural shape. This inward-forced curvature sharpens the pole, and the bending energy concentrated there grows with aspect ratio, so the pole becomes the dominant hotspot at high aspect ratio. The distributions in Fig. 6(d) make this handover explicit, with the energy concentrated at the junction at AR = 1 (3.3×10^{-3} MPa), balanced between the junction and the pole at the intermediate case near AR = 2 (3.7×10^{-3} MPa) where the two energy densities are equal, and concentrated at the pole at AR = 5 (2.5×10^{-2} MPa). This evolution from a junction-dominated to a pole-dominated energetic distribution precedes and accompanies the crossover from rim-dominated to shell-dominated buckling identified in Fig. 5(e). It is consistent with the nearly constant reverse buckling pressure at low aspect ratios and its subsequent decrease as shell-body deformation becomes increasingly important. The selected non-axisymmetric branch is examined directly through the Fourier decomposition below.

To characterize the development of the selected non-axisymmetric instability, the normal displacement was decomposed into circumferential Fourier modes after removing its axisymmetric component at each meridional position. Here, n denotes the circumferential Fourier mode number, or the number of oscillations around the circumference. The normalized RMS amplitudes A_n^{RMS}/t for modes $n = 3$–9 are presented in Supplementary Fig. S2.

The modal histories reveal that mode selection develops through competition during the loading path rather than through the exclusive presence of a single mode from the outset. In all representative calculations, the $n = 4$ component is the leading non-axisymmetric component through most of the prebuckling response. For the lower-aspect-ratio rimmed shells, however, the $n = 8$ component undergoes a rapid amplification immediately before the first limit point and overtakes $n = 4$, producing the eight-lobed instability observed at buckling. This late $n = 8$ amplification is observed for AR = 1 and 1.6 during forward inversion [Supplementary Fig. S2(a, b)] and for AR = 1 and 2.2 during reverse inversion [Supplementary Fig. S2(e, f)].

At higher aspect ratios, the $n = 8$ component does not overtake the pre-existing $n = 4$ component before instability. The $n = 4$ component instead continues its growth and develops into the selected buckling mode, as observed for AR = 1.7 and 3 during forward inversion [Supplementary Fig. S2(c, d)] and for AR = 2.4 and 3 during reverse inversion [Supplementary Fig. S2(g, h)]. The representative rimless shells [Supplementary Fig. S2(i–l)] exhibit the same persistent $n = 4$-dominated development without the late amplification of $n = 8$.

Combined with the SENER results, these modal histories suggest that the substantial rim deformation accumulated in the lower-aspect-ratio shells promotes the late growth of the competing $n = 8$ branch. As the aspect ratio increases, the shell reaches its intrinsic instability at a lower pressure, before the rim-induced $n = 8$ component can overtake the already leading $n = 4$ component. The observed rim-to-shell crossover is therefore characterized by whether the late $n = 8$ amplification becomes dominant before the first limit point. This criterion places the change in the selected mode between AR = 1.6 and 1.7 for forward inversion and between AR = 2.2 and 2.4 for reverse inversion, consistent with the critical aspect ratios of 1.7 and 2.4 at which the rimmed buckling-pressure curves change slope in Fig. 5(a) and 5(b).

8. Numerical study of post-buckling and inversion

8.1. *Effect of aspect ratio on post-buckling behaviors*

Fig. 7 illustrates the pole displacement as a function of normalized pressure with the corresponding post-buckling morphologies. Fig. 7(a) presents the pole displacement responses at T = 10 for both inversion processes, and Fig. 7(b) and (c) show the corresponding forward and reverse post-buckling morphologies at T = 1, respectively. The pole displacement responses are interpreted with the corresponding morphologies to clarify the detailed physics of the observed post-buckling behavior. For the forward inversion process, the responses can be classified into three distinct regions depending on the aspect ratio.

In Region I, the pole displacement drops sharply and monotonically from buckling onset until the complete inversion occurs [Fig. 7(a)], indicating that the structure proceeds toward inversion without noticeable contact during the propagation of buckling. The morphologies in Fig. 7(b) provide insight into this behavior. Following rim-dominated buckling, the dimples grow and compete until the deformation localizes into a single dominant dimple, which directly leads to complete inversion without noticeable contact.

In Region II, the pole displacement deviates from the simple monotonic trend observed in Region I, exhibiting a local minimum before complete inversion [Fig. 7(a)]. In the corresponding morphologies in

Fig. 7(b), two dimples form a transient internal contact near the pole before the deformation eventually localizes into a single dominant dimple and triggers complete inversion. This transient inner-surface self-contact gives rise to the observed local minimum but does not sustain an intermediate state that appreciably delays complete inversion.

In Region III, the pole displacement exhibits more complex behavior, and the pressure interval between the buckling onset and complete inversion becomes significantly wider [Fig. 7(a)]. The corresponding morphologies in Fig. 7(b) show that shell-dominated buckling localizes deformation in the mid-height region, leading to the formation of extensive inner-surface self-contact between the two remaining dimples. As post-buckling progresses, this self-contact propagates vertically and eventually merges into a unified body. The body remains connected to the rim through an outward-protruding folding structure, which resists further deformation until it eventually folds inward and triggers the onset of complete inversion. Following this transition, the outer surface of the shell, already in contact with the rim, slides against both the rim and itself along the meridional direction until complete inversion is achieved. These observations reveal that a modest drop in pole displacement immediately after buckling onset is followed by a gradual decrease over a substantial pressure interval as inner-surface self-contact develops and propagates within the shell. In addition, a large local minimum observed just before the complete inversion corresponds to the outer-surface self-contact formed between the shell and the rim. Furthermore, in these frictionless simulations, the wide pressure interval between buckling onset and complete inversion is associated primarily with the structural resistance of the intermediate state formed by inner-surface self-contact, whereas the subsequent outer-surface contact is followed by only a modest further increase in pressure. As a result, despite exhibiting much earlier buckling onset, shells with high aspect ratios still exhibit complete inversion pressures comparable to those of the other cases.

In Region IV, which covers the entire reverse inversion process, the responses are similar across all aspect ratios. As shown in Fig. 7(a), the pole displacement varies smoothly and monotonically during the reverse inversion process regardless of the aspect ratio. Furthermore, as shown in Fig. 7(c), despite the shells initiating collapse through different buckling modes, inversion is observed to initiate from the shell–rim junction before the differences in shell deformation associated with the two buckling modes become pronounced. The inversion subsequently propagates sequentially toward the pole, ultimately leading to complete inversion.

8.2. *Effect of friction on complete inversion pressure*

To explicitly isolate the intrinsic elastic and geometric responses of the shell from the effects of interfacial friction, we simulate the frictionless limit, in which the shell slides freely against the rim and against itself. This idealized baseline is then compared with both the lubricated and non-lubricated experiments to assess the role of interfacial resistance in the complete inversion pressure, its aspect-ratio dependence, and the corresponding deformation pathway. Quantitative finite-friction prediction requires interface-specific calibration and validation during large deformation, evolving self-contact, and sliding against the rim; the measured effective coefficient alone does not establish the appropriate friction law for these contact states, such as a constant-coefficient Coulomb law or a law whose coefficient depends on contact pressure and sliding rate. This contact-model validation is beyond the present study, which uses the frictionless limit to separate the geometric and structural effects of the shell, rim, and self-contact.

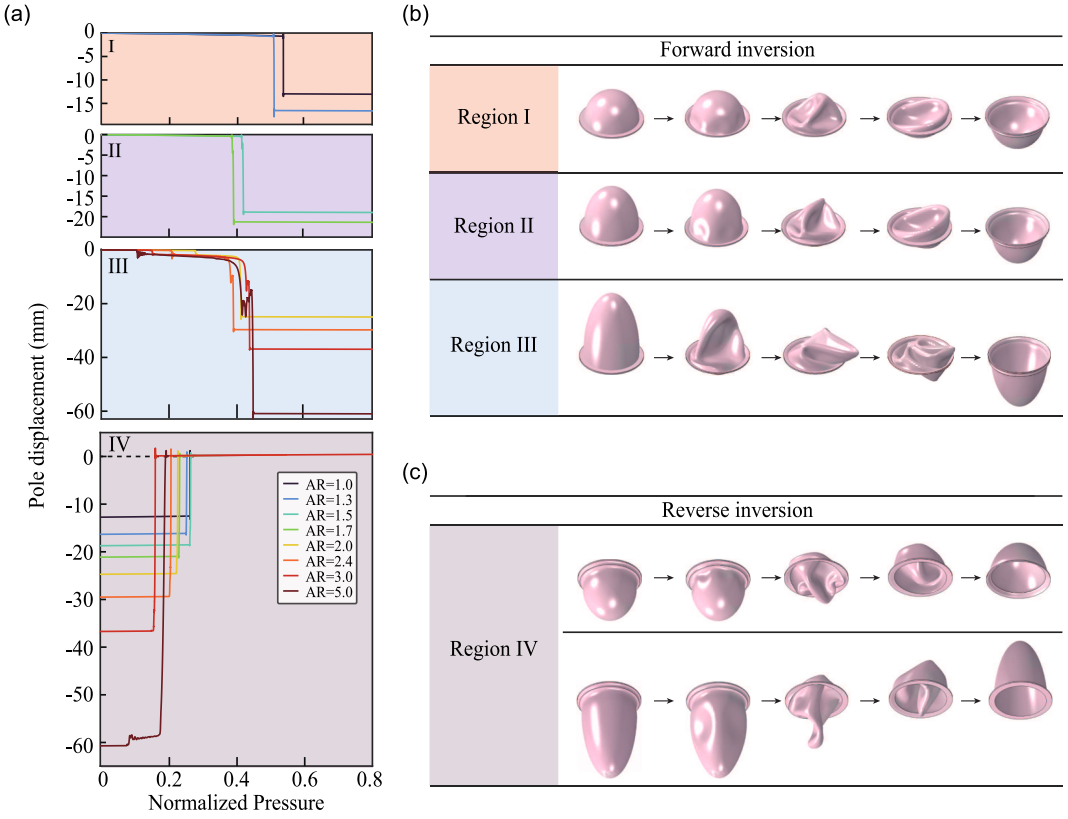

Fig. 7. Post-buckling behavior and pole-displacement responses for various aspect ratios. (a) Pole displacement versus normalized pressure, calculated with a step time of T = 10, during the forward inversion, classified into three regions (I, II, and III), and during the reverse inversion, which forms a single Region IV. The line color denotes the aspect ratio from AR = 1.0 to 5.0 as given in the legend, and the black dashed line in Region IV marks zero pole displacement. (b) Representative forward post-buckling morphologies for Region I (AR = 1.1), Region II (AR = 1.5), and Region III (AR = 2.4) at a step time of T = 1. (c) Representative reverse post-buckling morphologies for Region IV, shown for AR = 1.5 and AR = 3.0 at a step time of T = 1.

Fig. 8(a) compares the normalized complete inversion pressure of the forward inversion against aspect ratio for the non-lubricated and lubricated experiments and the frictionless simulation at T = 10, with the corresponding morphological evolution in Fig. 8(b). The lubricated experiments exhibit only weak dependence on aspect ratio, with a mean normalized complete-inversion pressure of approximately 0.521 ± 0.047. A similarly weak aspect-ratio dependence is observed in the frictionless simulations at higher aspect ratios. At low aspect ratios, the complete-inversion pressure retains a noticeable aspect-ratio dependence because complete inversion can occur only after the initial buckling instability, whose critical pressure varies strongly with aspect ratio. As the aspect ratio increases and the buckling pressure falls below the pressure required to propagate inversion, the complete-inversion pressure approaches a nearly aspect-ratio-independent level. The non-lubricated shells, by contrast, require substantially higher pressures that grow with aspect ratio, because the enlarging contact area between the everting shell, the rim, and itself adds frictional resistance that must be overcome to complete inversion.

Fig. 8(c) shows the same comparison for the reverse inversion, with the morphologies in Fig. 8(d), and the lubricated experiments show only weak aspect ratio dependence, with a mean normalized pressure of 0.285 ± 0.013. The frictionless simulations show the same overall tendency. As in the forward inversion process, the remaining offset between the lubricated experiments and the frictionless simulations is consistent with the finite interfacial resistance retained at the lubricated interface. The reverse inversion pressure is markedly lower than the forward value, leaving a lubricated gap of approximately 0.16–0.28 across aspect ratios [Fig. 8(a) and 8(c)]. This asymmetry is structural. The shell is molded in its natural, non-everted shape, so returning from the everted state is energetically favorable, and the reverse inversion proceeds smoothly by initiating at the shell–rim junction and propagating toward the pole, as captured by the single Region IV behavior in Fig. 7. The forward inversion, by contrast, must force the shell out of its preferred shape through dimpling and extensive self-contact, which demands a higher pressure. Under non-lubricated conditions, this gap narrows at high aspect ratios, falling to about 0.04 at AR = 4, because friction raises the reverse pressure toward the forward value as the contact area grows and the two pathways come to resemble each other.

The morphological sequences in Fig. 8(b) and (d) reveal how friction enters the inversion. As the shell collapses, it first forms inner-surface self-contact and then, in the later stages, slides against the rim and against its own outer surface along the meridional direction. Inner-surface self-contact provides structural support during inversion. The additional resistance under non-lubricated conditions becomes pronounced during the later outer-surface sliding stage [Fig. 8(b, d)], and the complete-inversion pressure increases with aspect ratio as the outer contact area enlarges. The effect is most dramatic in the reverse process. Under lubrication, the shell inverts symmetrically by propagating from the junction to the pole, but without lubrication, the suppressed sliding prevents small misalignments from relaxing, so they accumulate into a pronounced asymmetric tilt. The tilted shell leans against the rim and develops the same extensive outer-surface contact seen in the forward process, raising the pressure needed to complete inversion at AR = 3 to approximately twice the lubricated value and about 3.7 times the frictionless value [Fig. 8(c)]. This tilting recurs in other high-aspect-ratio shells (AR = 4 and 5) and, by making the two pathways increasingly alike, explains why the non-lubricated forward and reverse pressures converge at high aspect ratios.

9. Conclusions

This work combines experiments and finite element simulations to examine how pressure-actuated oval shells buckle and invert, focusing on three factors, namely aspect-ratio-dependent shell geometry, the rim boundary, and interfacial friction. The buckling pressure of a rimmed shell does not decrease uniformly with aspect ratio but changes slope at a critical aspect ratio, distinct for the forward and reverse processes, where the governing buckling mode shifts from rim-dominated to shell-

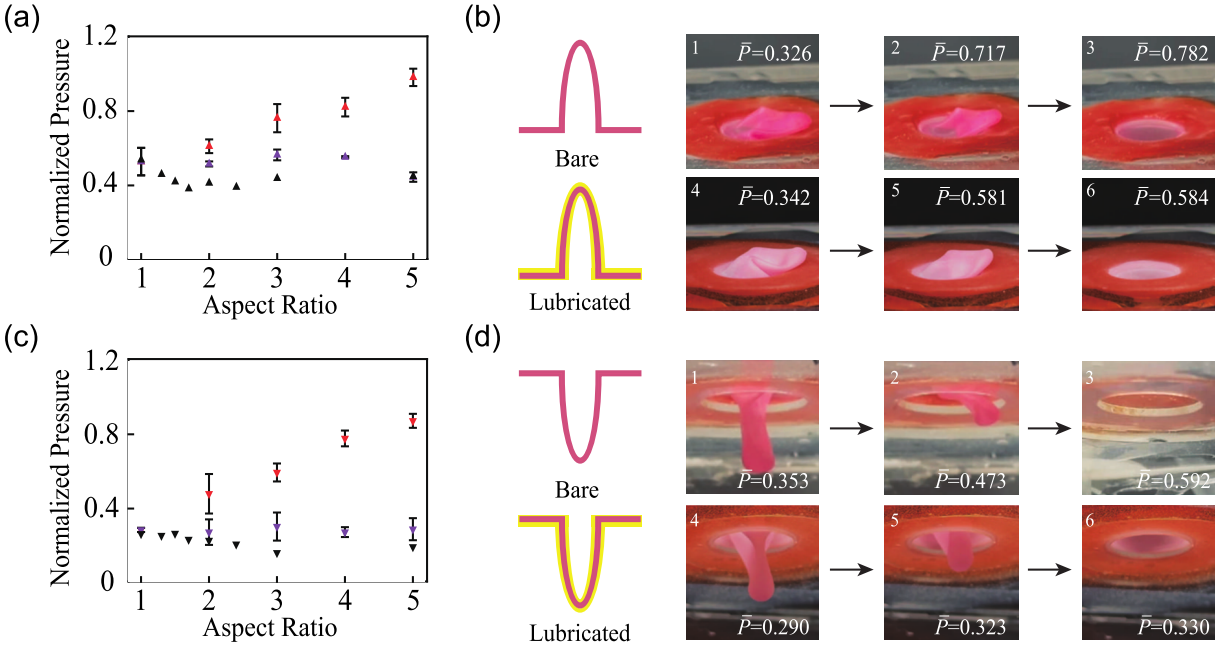

Fig. 8. Effect of interfacial friction on the complete inversion pressure and post-buckling morphology. (a) Normalized complete inversion pressure versus aspect ratio during forward inversion for the non-lubricated (red) and lubricated (purple) experiments and the frictionless simulation with a step time of T = 10 (black), with error bars denoting ± 1 SD from three independent shell specimens. (b) Forward post-buckling morphologies of a bare and a lubricated shell (AR = 3), with stages 1 to 3 for the bare shell and 4 to 6 for the lubricated shell and the corresponding normalized pressures. (c) Normalized complete inversion pressure versus aspect ratio during reverse inversion, with the same color scheme as in (a). (d) Reverse post-buckling morphologies of a bare and a lubricated shell (AR = 3), labeled as in (b). In both (b) and (d), the lubricated shell completes inversion at a lower pressure than the bare shell. The cross-sectional schematics distinguish the bare shell from the lubricated shell coated with a thin lubricant layer.

dominated. Comparison with the rimless shells, together with the strain-energy and Fourier modal analyses, identifies the supporting rim as the origin of the crossover in the buckling response. The $n = 4$ component is the leading non-axisymmetric component through most of the pre-buckling loading path in the examined reference calculations. At low aspect ratios, the relatively high intrinsic buckling resistance allows substantial rim deflection and junction loading to accumulate before instability. Under these conditions, the competing $n = 8$ component undergoes rapid amplification immediately before the limit point and overtakes $n = 4$, producing the observed rim-dominated eight-lobed mode. At higher aspect ratios, the shell reaches its intrinsic instability at a lower pressure, before this late $n = 8$ amplification can become dominant, and the pre-existing $n = 4$ component develops into the selected shell-dominated mode.

Beyond the onset of buckling, the post-buckling response sets the complete inversion pressure. In the lubricated experiments and frictionless simulations, its overall dependence on aspect ratio is weaker than that of the buckling pressure, despite the earlier buckling of slender shells. In the forward process, this insensitivity arises because extensive self-contact formed during inversion builds a temporary load-bearing structure that sustains the pressure, while in the reverse process, inversion initiates at the shell–rim junction and propagates smoothly to the pole. The reverse inversion pressure stays well below the forward value because the shell returns to its molded shape, which is energetically favorable. Interfacial friction then governs the magnitude of these pressures. Both the lubricated experiments and the ideal frictionless simulations exhibit comparatively low pressures and weak overall dependence on aspect ratio, while the remaining offset between them is consistent with the finite interfacial resistance retained under lubrication. In contrast, the non-lubricated shells experience greater resistance to interfacial sliding, develop asymmetric tilting and extensive outer-surface contact, and require markedly higher pressures that narrow the forward–reverse asymmetry. Together, these results clarify how aspect-ratio-dependent shell geometry, the rim boundary, and friction set the buckling and inversion of curved shells, and they provide potential design implications for pressure-actuated shell-based soft machines.

These results also point to a potential role for oval geometry in bistable soft devices. Compared with a hemispherical shell of the same base radius, a prolate oval shell offers a larger pole stroke and a different axial contact geometry. In the frictionless forward simulations, a Region I shell with an aspect ratio near 1.3 inverts at a lower pressure while delivering a longer stroke than the hemispherical dome [Fig. 7(a)], which could be advantageous for soft actuators that convert a slow pneumatic input into a fast mechanical output (Rothemund et al., 2018). The larger enclosed volume increases the volume swept between the two stable states and could potentially increase the output of bistable soft pumps (Buranabunwong, 2024; Wen, 2025). The different axial contact geometry may also be relevant to bistable check-valve designs (Buranabunwong, 2024). Looking further ahead, replacing the passive rim with a stimulus-responsive material would allow the shell to invert in response to a local environmental signal such as pH or temperature, rather than through an external pressure line. These potential benefits remain to be tested experimentally.

CRediT authorship contribution statement

Haesoo Park: Writing – original draft, Visualization, Investigation. **Yuseong Song:** Writing – original draft, Methodology, Investigation, Formal analysis, Data curation. **Kanghyun Ki:** Methodology, Investigation, Data curation. **Anna Lee:** Writing – review & editing, Writing – original draft. **Jonghyun Ha:** Writing – review & editing, Writing – original draft, Conceptualization.

Declaration of competing interest

The authors declare that they have no known competing financial interests or personal relationships that could have appeared to influence the work reported in this paper.

Acknowledgement

This work was supported by the National Research Foundation of Korea (NRF) grant funded by the Korea government (No. RS-2024-00341444 and RS-2024-00349732).

Appendix A. Supplementary data

Supplementary data to this article can be found online at https://doi.org/10.1016/j.ijsolstr.2026.114424.

Data availability

The data that support the findings of this study are available from the corresponding author upon reasonable request.

References

Arbocz, J., Babcock Jr., C.D., 1969. The effect of General Imperfections on the Buckling of Cylindrical Shells. J. Appl. Mech. 36, 28–38.
Armon, S., Efrati, E., Kupferman, R., Sharon, E., 2011. Geometry and Mechanics in the opening of Chiral seed Pods. Science 333, 1726–1730.
Barber, J.R., Ciavarella, M., 2000. Contact mechanics. Int. J. Solids Struct. 37, 29–43.
Bende, N.P., Evans, A.A., Innes-Gold, S., Marin, L.A., Cohen, I., Hayward, R.C., Santangelo, C.D., 2015. Geometrically controlled snapping transitions in shells with curved creases. PNAS 112, 11175–11180.
Berthold, R., Burgner-Kahrs, J., Wangenheim, M., Kahms, S., 2023. Investigating frictional contact behavior for soft material robot simulations. Meccanica 58, 2165–2176.
Boiko, D.V., Zheleznov, L.P., Kabanov, V.V., 2009. Studies of nonlinear deformation and stability of oval and elliptic cylindrical shells under axial compression. Mech. Solids 44, 762–768.
Boley, J.W., van Rees, W.M., Lissandrello, C., Horenstein, M.N., Truby, R.L., Kotikian, A., Lewis, J.A., Mahadevan, L., 2019. Shape-shifting structured lattices via multimaterial 4D printing. PNAS 116, 20856–20862.
Brinkmeyer, A., Santer, M., Pirrera, A., Weaver, P.M., 2012. Pseudo-bistable self-actuated domes for morphing applications. Int. J. Solids Struct. 49, 1077–1087.
Buranabunwong, C., et al., 2024. Magnetic bistable dome actuators for soft robotics with high volume capacity and motion stability. ACS Appl. Mater. Interfaces 17, 3930–3940.
Chen, T., Bilal, O.R., Shea, K., Daraio, C., 2018. Harnessing bistability for directional propulsion of soft, untethered robots. PNAS 115, 5698–5702.
Chen, Z., Guo, Q., Majidi, C., et al., 2012. Nonlinear geometric effects in bistable structures. Phys. Rev. Lett. 109, 114302.
Choe, J.K., Kim, J., Song, H., Bae, J., Kim, J., 2023. A soft, self-sensing tensile valve for perceptive soft robots. Nat. Commun. 14, 3942.
Cottone, F., Vocca, H., Gammaitoni, L., 2009. Nonlinear energy harvesting. Phys. Rev. Lett. 102, 080601.
Durak, G.M., Speck, T., Poppinga, S., 2022. Shapeshifting in the Venus flytrap (*Dionaea muscipula*): Morphological and biomechanical adaptations and the potential costs of a failed hunting cycle. Front. Plant Sci. 13, 970320.
Esser, F.J., Auth, P., Speck, T., 2020. Artificial Venus flytraps: a Research Review and Outlook on their Importance for Novel Bioinspired Materials Systems. Front. Robot. AI 7, 75.
Feinstein, G., Erickson, B., 1971. Jacob Kempner, Stability of oval cylindrical shells. Exp. Mech. 11, 514–520.
Forterre, Y., Skotheim, J.M., Dumais, J., Mahadevan, L., 2005. How the Venus flytrap snaps. Nature 433, 421–425.
Gomez, M., Moulton, D.E., Vella, D., 2017. Critical slowing down in purely elastic snap-through instabilities. Nat. Phys. 13, 142–145.
Gomez, M., Moulton, D.E., Vella, D., 2019. Dynamics of viscoelastic snap-through. J. Mech. Phys. Solids 124, 781–813.
Gorissen, B., Melancon, D., Vasios, N., Torbati, M., Bertoldi, K., 2020. Inflatable soft jumper inspired by shell snapping. Sci. Rob. 5, eabb1967.
Guest, S.D., Pellegrino, S., 2006. Analytical models for bistable cylindrical shells. Proc. R. Soc. A 462, 839–854.
Haas, P.A., Goldstein, R.E., 2018. Embryonic inversion in Volvox carteri: the flipping and peeling of elastic lips. Phys. Rev. E 98, 052415.
Harne, R.L., Wang, K.W., 2013. A review of the recent research on vibration energy harvesting via bistable systems. Smart Mater. Struct. 22, 023001.
Hayashi, M., Feilich, K.L., Ellerby, D.J., 2009. The mechanics of explosive seed dispersal in orange jewelweed (*Impatiens capensis*). J. Exp. Bot. 60, 2045–2053.

Hofhuis, H., Moulton, D., Lessinnes, T., Routier-Kierzkowska, A.-L., Bomphrey, R.J., Hay, A., 2016. Morphomechanical Innovation Drives Explosive seed Dispersal. Cell 166, 222–233.
Höhn, S., Honerkamp-Smith, A.R., Haas, P.A., Khuc Trong, P., Goldstein, R.E., 2015. Dynamics of a Volvox embryo turning itself inside out. Phys. Rev. Lett. 114, 178101.
Huang, W., Liu, Z., Liu, M., Hsia, K.J., 2024. Snap-through eversion of axisymmetric shells under contact indentation. Proc. R. Soc. A 480, 20240303.
Hutchinson, J.W., 1967. Imperfection sensitivity of externally pressurized spherical shells. J. Appl. Mech. 34, 49–55.
Hutchinson, J.W., 2016. Buckling of spherical shells revisited. Proc. R. Soc. A 472, 20160577.
Hutchinson, J.W., Koiter, W.T., 1970. Postbuckling Theory. Appl. Mech. Rev. 23 (12), 1353–1366.
Kendall, K., 1975. Thin-film peeling—the elastic term. J. Phys. D Appl. Phys. 8, 1449–1452.
Kim, C., Shin, C., Lee, A., Ha, J., Choi, J., 2025. Bistable magnetic valves for selective sweat sampling in wearable microfluidics. Lab Chip 25, 5180–5188.
Kim, J., Hanna, J.A., Byun, M., Santangelo, C.D., Hayward, R.C., 2012. Designing responsive buckled surfaces by halftone gel lithography. Science 335, 1201–1205.
Liu, M., Domino, L., Dupont de Dinechin, I., Taffetani, M., Vella, D., 2023. Snap-induced morphing: from a single bistable shell to the origin of shape bifurcation in interacting shells. J. Mech. Phys. Solids 170, 105116.
Liu, Y., Pan, F., Xiong, F., Wei, Y., Ruan, Y., Ding, B., Yang, K., Chen, Y., 2023. Ultrafast shape-reconfigurable chiral mechanical metamaterial based on prestressed bistable shells. Adv. Funct. Mater. 33, 2300433.
Mallol, P., Mao, H., Tibert, G., 2018. Experiments and simulations of the deployment of a bistable composite boom. J. Spacecr. Rocket. 55, 1–11.
Mosadegh, B., Kuo, C.H., Tung, Y.C., Torisawa, Y.S., Bersano-Begey, T., Tavana, H., Takayama, S., 2010. Integrated elastomeric components for autonomous regulation of sequential and oscillatory flow switching in microfluidic devices. Nat. Phys. 6, 433–437.
Norman, A.D., Seffen, K.A., Guest, S.D., 2008. Multistable corrugated shells. Proc. R. Soc. A 464, 1653–1672.
Pellegrini, S.P., Tolou, N., Schenk, M., Herder, J.L., 2013. Bistable vibration energy harvesters: a review. J. Intell. Mater. Syst. Struct. 24, 1303–1312.
Persson, B.N.J., 2001. Theory of rubber friction and contact mechanics. J. Chem. Phys. 115, 3840–3861.
Pezzulla, M., Stoop, N., Steranka, M.P., Bade, A.J., Holmes, D.P., 2018. Curvature-induced instabilities of shells. Phys. Rev. Lett. 120, 048002.
Pietrzak, G., Curnier, A., 1999. Large deformation frictional contact mechanics: continuum formulation and augmented Lagrangian treatment. Comput. Methods Appl. Mech. Eng. 177, 351–381.
Pirrera, A., Avitabile, D., Weaver, P.M., 2010. Bistable plates for morphing structures: a refined analytical approach with high-order polynomials. Int. J. Solids Struct. 47, 3412–3425.
Qiao, C., Liu, L., Pasini, D., 2021. Bi-shell valve for fast actuation of soft pneumatic actuators via shell snapping interaction. Adv. Sci. 8, 2100445.
Raney, J.R., Nadkarni, N., Daraio, C., Kochmann, D.M., Lewis, J.A., Bertoldi, K., 2016. Stable propagation of mechanical signals in soft media using stored elastic energy. PNAS 113, 9722–9727.
Rothemund, P., Ainla, A., Belding, L., Preston, D.J., Kurihara, S., Suo, Z., Whitesides, G. M., 2018. A soft, bistable valve for autonomous control of soft actuators. Sci. Rob. 3, eaar7986.
Schenk, M., Guest, S.D., 2014. On zero stiffness. Proceedings of the Royal Society A 470, 20130648.
Seffen, K.A., 2007. 'Morphing' bistable orthotropic elliptical shallow shells. Proceedings of the Royal Society A 463, 67–83.
Seffen, K.A., Pellegrino, S., 1999. Deployment dynamics of tape springs. Proc. R. Soc. A 455, 1003–1048.
Shan, S., Kang, S.H., Raney, J.R., et al., 2015. Multistable Architected Materials for Trapping Elastic Strain Energy. Adv. Mater. 27, 4296–4301.
Shariati, M., Mahdizadeh Rokhi, M., 2010. Buckling of steel cylindrical shells with elliptical cutout. Int. J. Steel Struct. 10, 193–205.
Shi, J., Mofatteh, H., Mirabolghasemi, A., et al., 2021. Programmable Multistable Perforated Shellular. Adv. Mater. 33, 2102423.
Silvestre, N., 2008. Buckling behaviour of elliptical cylindrical shells and tubes under compression. Int. J. Solids Struct. 45, 4427–4447.
Sobota, P.M., Seffen, K.A., 2019. Bistable polar-orthotropic shallow shells. R. Soc. Open Sci. 6, 190888.
Stanton, S.C., McGehee, C.C., Mann, B.P., 2009. Reversible hysteresis for broadband magnetopiezoelastic energy harvesting. Appl. Phys. Lett. 95, 174103.
Taffetani, M., Jiang, X., Holmes, D.P., Vella, D., 2018. Static bistability of spherical caps. Proc. R. Soc. A 474, 20170910.
Tang, Y., Chi, Y., Sun, J., Huang, T.H., Maghsoudi, O.H., Spence, A., Zhao, J., Su, H., Yin, J., 2020. Leveraging elastic instabilities for amplified performance: Spine-inspired high-speed and high-force soft robots. Sci. Adv. 6, 6912.
Tennyson, R.C., Booton, M., Caswell, R.D., 1971. Buckling of imperfect elliptical cylindrical shells under axial compression. AIAA J. 9, 250–255.
Tvergaard, V., 1976. Buckling of elastic-plastic oval cylindrical shells under axial compression. Int. J. Solids Struct. 12, 683–691.
Vakis, A., Yastrebov, V.A., Scheibert, J., et al., 2018. Modeling and simulation in tribology across scales: an overview. Tribol. Int. 125, 169–199.
Vella, D., Ajdari, A., Vaziri, A., Boudaoud, A., 2012. The indentation of pressurized elastic shells: from polymeric capsules to yeast cells. J. R. Soc. Interface 9, 448–455.
Vidoli, S., Maurini, C., 2008. Tristability of thin orthotropic shells with uniform initial curvature. Proceedings of the Royal Society A 464, 2949–2966.
Volkov, A.G., Adesina, T., Jovanov, E., 2007. Closing of Venus flytrap by electrical stimulation of motor cells. Plant Signal. Behav. 2, 139–145.
Wen, H., et al., 2025. Magnetoactive bistable soft actuators for programmable large shape transformations at low magnetic fields. Nat. Commun. 16, 9714.
Xu, R., Chen, C., Sun, J., He, Y., Li, X., Lu, M.-H., Chen, Y., 2023. The design, manufacture and application of multistable mechanical metamaterials—A state-of-the-art review. Int. J. Extrem. Manuf. 5, 042013.
Zhang, J., Zhang, M., Tang, W., Wang, W., Wang, M., 2017. Buckling of prolate egg-shaped domes under hydrostatic external pressure. Thin-Walled Struct. 119, 296–303.
Zhang, Z., Xu, J., Ma, Y., Sun, M., Pan, B., Chai, H., Zhang, G., Jiang, S., 2023. Morphing characteristics and damage analysis of 3D printing variable stiffness bistable laminates based on continuous fiber thermosetting composites. Compos. Struct. 315, 117026.
Zoelly, R., 1915. *Ueber ein Knickungsproblem an der Kugelschale*, Doctoral Thesis. ETH Zürich, Zürich.